Optical Signatures of Coupled Quantum Dots

E. A. Stinaff,[1] M. Scheibner,[1] A. S. Bracker,[1] I. V. Ponomarev,[1] V. L. Korenev,[2] M. E. Ware,[1] M. F. Doty,[1] T. L. Reinecke,[1] D. Gammon[1]*

An asymmetric pair of coupled InAs quantum dots is tuned into resonance by applying an electric field so that a single hole forms a coherent molecular wave function. The optical spectrum shows a rich pattern of level anticrossings and crossings that can be understood as a superposition of charge and spin configurations of the two dots. Coulomb interactions shift the molecular resonance of the optically excited state (charged exciton) with respect to the ground state (single charge), enabling light-induced coupling of the quantum dots. This result demonstrates the possibility of optically coupling quantum dots for application in quantum information processing.

Semiconductor approaches to quantum information can leverage the industry's vast technological infrastructure and integrate with existing information and communication technologies. Quantum dots (QDs) are an attractive host for storing a quantum information bit (qubit), because their atom-like properties (1) can be engineered through modern nanofabrication and crystal growth techniques (2–5). Advances in the fabrication and physics of single quantum dots (SQDs), together with the need for scalable qubit arrays (6, 7), have recently brought coupled quantum dots (CQDs) to the foreground. Electron transport measurements on CQDs have demonstrated spin-sensitive coupling and manipulation of electron and nuclear spins (8–10), and optical spectra of coupled excitons have been measured (11–14) and calculated (15–19) in self-assembled CQDs.

Optical spectroscopy is a powerful tool for probing and manipulating QDs. Many of the methods of atomic physics can be used, including coherent manipulation (20, 21) and optical orientation (22–24). Although coupled excitons in a single QD have been used to demonstrate a two-qubit gate (21), an optical architecture ultimately requires long-lived qubits such as the spin of an unpaired electron (23, 24) or hole (25). This would then have the advantage that optically excited states could be used as auxiliary levels for ultrafast control of the qubits.

We present the optical spectrum of a CQD containing a single extra charge. In analogy with the transport systems (8–10) and with recent CQD exciton studies (13, 14), we use an applied electric field to convert between molecular and atomlike orbital states. Our experiments reveal a distinct molecular state for the extra charge alone and another for its optically excited state (trion, or singly charged exciton). Spin leads to well-resolved singlet and triplet transitions in the anticrossing region of the charged exciton.

[1]Naval Research Laboratory, Washington, DC 20375, USA. [2]A. F. Ioffe Physical Technical Institute, St. Petersburg 194021, Russia.

*To whom correspondence should be addressed. E-mail: gammon@nrl.navy.mil

Our InAs QDs are grown by molecular beam epitaxy using an indium flush technique (2, 3, 26). After a thin GaAs tunneling barrier of thickness d, a second layer of QDs nucleates preferentially above the first layer of dots, forming CQDs (4, 5). In some cases, the two dot layers are grown with substantially different heights to separate the optical transitions and to distinguish between the individual dots in an asymmetric CQD pair. The QDs are embedded in a n^+-intrinsic-Schottky diode (Fig. 1A) to apply an electric field and to control the charging (27). To study individual CQDs, photoluminescence (PL) was excited and detected at ~10 K through aluminum shadow masks with 1-μm-diameter apertures.

The PL energy dispersion as a function of applied field for SQDs and CQDs show marked differences (Fig. 2). Nevertheless, there are similarities in their electric field dependence, charging, and binding energies. The SQD pattern has been well understood as a series of excitons that shift discretely in energy as the charge state changes (27, 28). We identify the neutral exciton (X^0) (a single electron and hole), a positively charged exciton (X^{+1}) that contains an additional hole and lies within a few meV of X^0, and a series of negatively charged excitons starting with the negative trion (X^{-1}) ~ 6 meV to lower energy. This qualitative pattern of discrete energy shifts is also observed in the CQDs, as expected for direct recombination in the lower energy dot of an asymmetric CQD pair (Fig. 1B). Additionally, we observe transitions with large electric field dependences (Stark shifts) and intriguing patterns of crossings and anticrossings in Fig. 2, A and B.

The exciton energies and transitions for the lower energy dot ("B") of an asymmetric CQD pair are shown schematically as a function of electric field in Fig. 1C. Away from the crossing point, the direct recombination ($^{10}_{10}X^0$), which arises from the electron and hole recombining primarily in the same dot, has a weak Stark shift. In contrast, the indirect recombination ($^{10}_{01}X^0$) arising from the electron and hole localized on different dots (13, 14) displays a strong linear Stark shift, $\Delta E = e[d +$

$(h_B + h_T)/2)]F$, where the slope depends on barrier thickness (d) and where F is the electric field. When the direct and indirect transition energies of an asymmetric CQD approach each other, either the electron or hole levels in the two dots become resonant, the wave functions become delocalized over both dots, and the transitions show anticrossing behavior. Away from these anticrossings the wave functions retain their single dot character. The anticrossing splitting depends on the tunneling rates, which in turn depend on barrier thickness and carrier mass. For the neutral exciton, we observe an indirect transition with a strong Stark shift and an anticrossing (Δ_{X^0} in Fig. 2B), consistent with recent reports (13, 14).

The asymmetric nature of these CQDs simplifies our interpretation of their spectra, because electron and hole resonances occur at different fields and can therefore be considered independently. For these CQDs, the bottom dot ("B") has a smaller direct transition energy than the top dot ("T"), as represented in Fig. 1B.
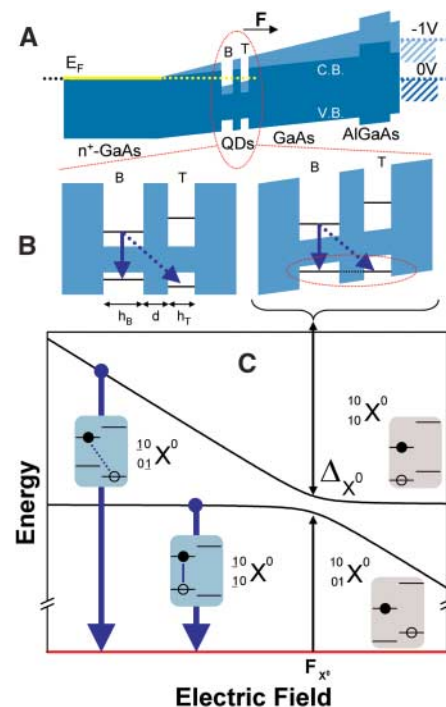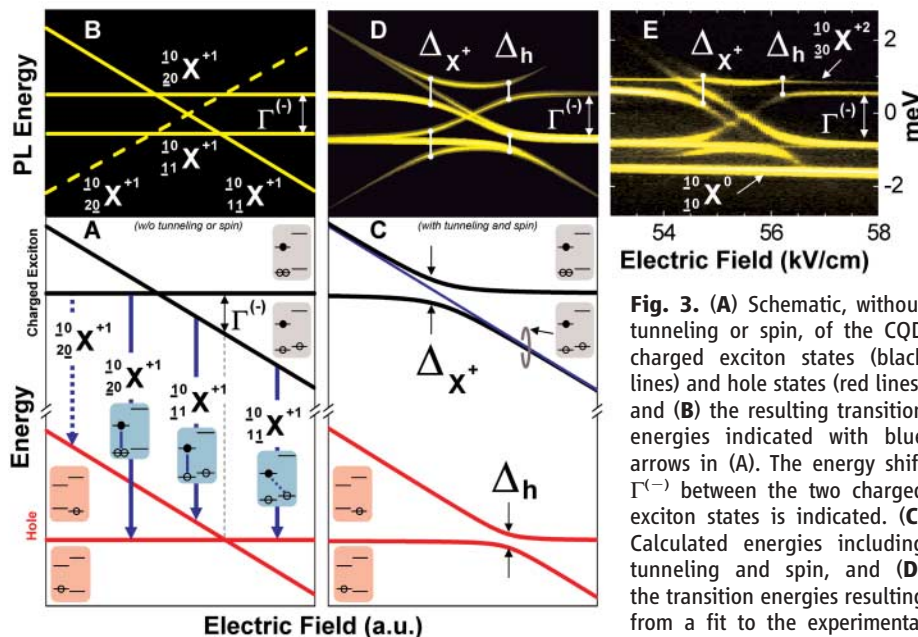

Fig. 1. (A) Band-edge diagram of the device layer structure. The two dots are labeled bottom (B) and top (T). Electric field direction, F, is also indicated. **(B)** Schematic of the CQD region at flat-band condition and at the field (F_{X^0}) where a hole resonance occurs. The direct (solid arrow) and indirect (dashed arrow) transitions are indicated. **(C)** Diagram of the X^0 initial state (black lines) and final state (red line, vacuum state) for dot B. The direct ($^{10}_{10}X^0$) and indirect ($^{10}_{01}X^0$) recombinations are indicated. The states are labeled $^{e_B e_T}_{h_B h_T}X^Q$, where the left superscripts (subscripts) give the number of electrons (holes) in the bottom e_B (h_B) and top e_T (h_T) dots and Q is the total charge of the system. The transitions are indicated by underlining the recombining carriers.

With this ordering, a larger electric field (higher reverse bias) brings the hole levels into resonance, whereas the electron levels become detuned and the electron remains localized (Fig. 1B, right). By inverting the order of the dots, i.e., smaller energy on top, we have been able to reverse this behavior and to observe the case of electron level resonance. For a CQD with a barrier thickness of 4 nm, we calculate and

measure electron anticrossing splittings that are an order of magnitude larger than for holes (e.g., 4.5 versus 0.42 meV). We discuss only results from samples with hole level resonances, such that the anticrossing energies are small (<1 meV), and the charging pattern in the molecule can be easily compared with that of SQDs.

Introducing a single additional charge into the CQD dramatically enriches the spectrum (Fig. 2,

box A), where we observe an intricate X-shape pattern with several anticrossing splittings close to 1 meV. The dominant features arise from a strong indirect transition ($_{11}^{10}X^{+1}$ with high Stark shift) that anticrosses two direct transitions ($_{20}^{10}X^{+1}$, $_{11}^{10}X^{+1}$ with small Stark shifts). There is also a weaker indirect transition of opposite slope that appears only between the anticrossings. Comparison with the electric field dependence of the SQD PL in Fig. 2 suggests that the spectral structure a few meV above $_{10}^{10}X^0$ results from a positively charged exciton state (positive trion). Anticrossings may occur only between states with the same total charge, so it follows that all of the features in this structure also arise from a positively charged exciton state (Fig. 2, box A). In contrast, the neutral exciton ($_{10}^{10}X^0$) passes unaffected through the anticrossing region of the positively charged exciton state. Similarly, $_{11}^{10}X^{+1}$ passes unaffected through the neutral exciton anticrossing region (Fig. 2, box B). To explain the details of the pattern in Fig. 2, box A, we now analyze the possible configurations for the three charges of a positively charged exciton in a coupled dot system.

We can understand the basic structure of the spectrum with a simplified energy-level diagram that does not include tunneling and spin (Fig. 3A). For a single hole there are two configurations (red lines), with the hole in one or the other of the dots. The charged exciton has six possible configurations (i.e., three particles in two dots), but the electron is localized in the bottom dot, so we need to consider only the hole configurations: Both holes can be in the top dot, both in the bottom dot, or one in each dot. The configuration with both holes in the top dot has a large Coulomb energy ($\Gamma^{(+)}$), because the holes are together and are separate from the electron. This puts its emission ~20 meV above the spectral range that we consider (26). On the other hand, the Coulomb energies of the other two configurations differ only by a small energy ($\Gamma^{(-)}$), which is the difference between the *e-h* attraction and *h-h* repulsion and amounts to a few meV. These two configurations are the initial states (black lines in Fig. 3A) that lead to our measured transitions.

The Coulomb energy shift ($\Gamma^{(-)}$) between the two charged exciton states is the essential origin of the X-shape in the PL spectrum (Fig. 3B). With two charged exciton states and two hole states, we have four PL transitions—two direct ($_{10}^{10}X^{+1}$, $_{11}^{10}X^{+1}$) and two indirect ($_{11}^{10}X^{+1}$, $_{20}^{10}X^{+1}$). The indirect transition, $_{20}^{10}X^{+1}$, is normally forbidden because both holes of the charged exciton are in a different dot than the final state hole. The direct PL transitions are separated by $\Gamma^{(-)}$, and the indirect transitions cross midway between them (Fig. 3B).

To add the effects of tunneling to this simple model, we have calculated the energies of the states and the resulting optical spectrum of asymmetric pairs of InGaAs/GaAs quantum dots having one electron and two holes (26). The

Fig. 2. Comparison of electric field–dependent photoluminescence spectra for a single QD (SQD) (left) and coupled QD (CQD) (right). We note the similarities such as field dependence, binding energies, and negative charging behavior, along with the observation of extraordinary Stark shift lines ($_{11}^{10}X^{+1}$, $_{01}^{10}X^0$), which show both crossing and anticrossing behavior. Box B shows the region of neutral exciton (X^0) anticrossing. Detail resulting from a positively charged exciton (X^+) in the CQD is displayed in box A. The insets are schematic cross sections of the two sample structures. CQD structures in this study are identified by the sequence of numbers $h_B/d/h_T$ corresponding to the height of the bottom dot, barrier thickness, and height of the top dot, all in nm. In this figure, the samples are ($h_B/d/h_T$) = (2.5/4/2.5) and for the SQD h = 3.5 nm. As in all figures, spectra are plotted as log(Intensity).

Fig. 3. (**A**) Schematic, without tunneling or spin, of the CQD charged exciton states (black lines) and hole states (red lines) and (**B**) the resulting transition energies indicated with blue arrows in (A). The energy shift $\Gamma^{(-)}$ between the two charged exciton states is indicated. (**C**) Calculated energies including tunneling and spin, and (**D**) the transition energies resulting from a fit to the experimental spectrum plotted in (**E**) for sample ($h_B/d/h_T$) = (4/4/2.5). With the introduction of tunneling and spin effects, we can see the two anticrossings events (Δ_h, Δ_{X^+}) which, along with $\Gamma^{(-)}$, give rise to the signature X-shape pattern. The parameters used to fit the data in (E) were $\Gamma^{(-)}$ = 1.27 meV and t = 1/2(Δ_h) = 0.23 meV. In (E), we note the two additional PL lines arising from the uncharged exciton ($_{10}^{10}X^0$) and the doubly positively charged exciton ($_{30}^{10}X^{+2}$). a.u., arbitrary units.

calculated energies are shown in Fig. 3C and the corresponding calculated spectrum in Fig. 3D. We have calculated the strength of the transitions using the matrix elements and assuming that the initial states are thermally distributed. Because of tunneling, we find that the transition $\frac{10}{20}X^{+1}$ becomes partially allowed. Moreover, tunneling produces delocalized molecular states only near the two fields where anticrossing is observed.

An important consequence of this energy level structure is that the molecular resonances for the hole and the charged exciton occur at different electric fields. This fact implies that there is a field where coupling between dots occurs only in the presence of optical excitation.

The inclusion of spin in the model leads to the identification of triplet states in the spectra. The $\frac{10}{20}X^{+1}$ emission results when both holes are in the s-shell of the same dot, where they must be in a spin singlet configuration, just as with a SQD. However, when the two holes are in separate dots, both singlet and triplet configurations arise. This is similar to the situation found in measurements of electron transport through double dots (8–10). Because tunneling (mainly) conserves spin (29), anticrossings will occur only for states with identical spin configurations, and the triplet states will not anticross with the singlet states. This results in a triplet state that passes through the anticrossing region unaltered (blue line in Fig. 3C) and appears as characteristic PL lines (Fig. 3D) that pass unaffected through the Δ_{X^+} anticrossing regions, providing a clear signature of a spin triplet. We

also observe fine structure in the spectra that indicates the presence of exchange interactions. Our theoretical description incorporates these effects (26), although detailed comparison with our predictions requires further investigation.

Good agreement is found between the calculated spectrum (Fig. 3D) and the measured spectrum (Fig. 3E), providing support for our model of coherent hole tunneling in a charged quantum dot molecule. Within our model, only two fitting parameters are necessary to reproduce the six observed PL lines: the difference in direct Coulomb energies ($\Gamma^{(-)}$) and the hole tunneling rate (t). Changing barrier thickness should lead to changes in the tunneling rate and the Stark shift of the indirect transition. We show that this is true in Fig. 4 for samples with barrier thicknesses of $d = 6$, 4, and 2 nm. Although the overall spectral pattern remains similar, we observe an obvious decrease in the slope (Stark shift) of the indirect PL line and an increase in the anticrossing energies, as expected. Although we find a large distribution of the anticrossing energies (e.g., for $d = 6$ nm, values of Δ_h vary from 0.23 to 0.55 meV), they show a systematic increase with decreasing barrier thickness. The values of $\Gamma^{(-)}$, however, range from 1 to 5 meV, with little obvious dependence on barrier thickness. This presumably arises from microscopic variations in structure (e.g., alloy composition, strain, etc.) but is not yet understood.

Comparing the anticrossing energies of the hole (Δ_h), the neutral exciton (Δ_{X^0}), and the charged exciton (Δ_{X^+}) reveals subtleties of the hole tunneling process. From these we obtain,

respectively, the tunneling rate of the hole by itself (t), in the presence of an electron, or in the presence of an e-h pair. The anticrossing energy of the hole is $\Delta_h = 2t$. For X^0, with an extra electron, it is increased to $\Delta_0 = 2(t + \delta_0)$, where δ_0 is an e-h Coulomb correction (26). For X^+, with an additional e-h pair, we obtain $\Delta_{X^+} = 2\sqrt{2}(t + \delta_+)$, where δ_+ is the correction to the Coulomb interaction between the hole and the extra e-h pair and is partially canceled and reduced with respect to δ_0. However, the overall rate is increased by $\sqrt{2}$ because now two holes can tunnel. From the CQD spectrum shown in Fig. 2, we measure $(\Delta_h, \Delta_{X^0}, \Delta_{X^+})_{4nm} = (0.60, 0.84, 0.89)$ meV, implying a tunneling rate of $t = 0.3$ meV and Coulomb corrections $(\delta_0, \delta_+) = (0.12, 0.02)$ meV.

We have shown that molecular resonance is achieved at different electric fields for the optically excited (trion) states and the ground (hole) states. This demonstrates that it is possible to bias the CQD so that the individual dots are not coupled except during optical excitation—potentially an important observation, because it provides the opportunity to use optical resonance to couple two dots only during the duration of an ultrashort laser pulse.

References and Notes

1. D. Gammon, D. G. Steel, *Phys. Today* **55**, 36 (2002).
2. J. M. Garcia et al., *Appl. Phys. Lett.* **71**, 2014 (1997).
3. Z. R. Wasilewski, S. Fafard, J. P. McCaffrey, *J. Cryst. Growth* **201–202**, 1131 (1999).
4. Q. Xie, A. Madhukar, P. Chen, N. P. Kobayashi, *Phys. Rev. Lett.* **75**, 2542 (1995).
5. G. S. Solomon, J. A. Trezza, A. F. Marshall, J. S. Harris Jr., *Phys. Rev. Lett.* **76**, 952 (1996).
6. P. Chen, C. Piermarocchi, L. J. Sham, *Phys. Rev. Lett.* **87**, 067401 (2001).
7. E. Biolatti, R. C. Iotti, P. Zanardi, F. Rossi, *Phys. Rev. Lett.* **85**, 5647 (2000).
8. F. H. L. Koppens et al., *Science* **309**, 1346 (2005).
9. J. R. Petta et al., *Science* **309**, 2180 (2005).
10. T. Hatano, M. Stopa, S. Tarucha, *Science* **309**, 268 (2005).
11. G. Schedelbeck, W. Wegscheider, M. Bichler, G. Abstreiter, *Science* **278**, 1792 (1997).
12. M. Bayer et al., *Science* **291**, 451 (2001).
13. H. J. Krenner et al., *Phys. Rev. Lett.* **94**, 057402 (2005).
14. G. Ortner et al., *Phys. Rev. Lett.* **94**, 157401 (2005).
15. Y. Lyanda-Geller, T. L. Reinecke, M. Bayer, *Phys. Rev. B* **69**, 161308 (2004).
16. J. M. Villas-Boas, A. O. Govorov, S. E. Ulloa, *Phys. Rev. B* **69**, 125342 (2004).
17. D. Bellucci, F. Troiani, G. Goldoni, E. Molinari, *Phys. Rev. B* **70**, 205332 (2004).
18. G. Bester, A. Zunger, J. Shumway, *Phys. Rev. B* **71**, 075325 (2005).
19. B. Szafran et al., *Phys. Rev. B* **71**, 205316 (2005).
20. A. Zrenner et al., *Nature* **418**, 612 (2002).
21. X. Q. Li et al., *Science* **301**, 809 (2003).
22. S. Cortez et al., *Phys. Rev. Lett.* **89**, 207401 (2002).
23. M. Kroutvar et al., *Nature* **432**, 81 (2004).
24. A. S. Bracker et al., *Phys. Rev. Lett.* **94**, 047402 (2005).
25. L. M. Woods, T. L. Reinecke, R. Kotlyar, *Phys. Rev. B* **69**, 125330 (2004).
26. Details of the experiment and calculations can be found in the Supporting Online Material on *Science* Online.
27. R. J. Warburton et al., *Nature* **405**, 926 (2000).
28. M. E. Ware et al., *Phys. Rev. Lett.* **95**, 177403 (2005).
29. This is only approximate; asymmetric h-h and e-h exchange will mix slightly the singlet and triplet states. Recently, it has been shown in electronic manipulation of charged molecules that hyperfine interactions can flip

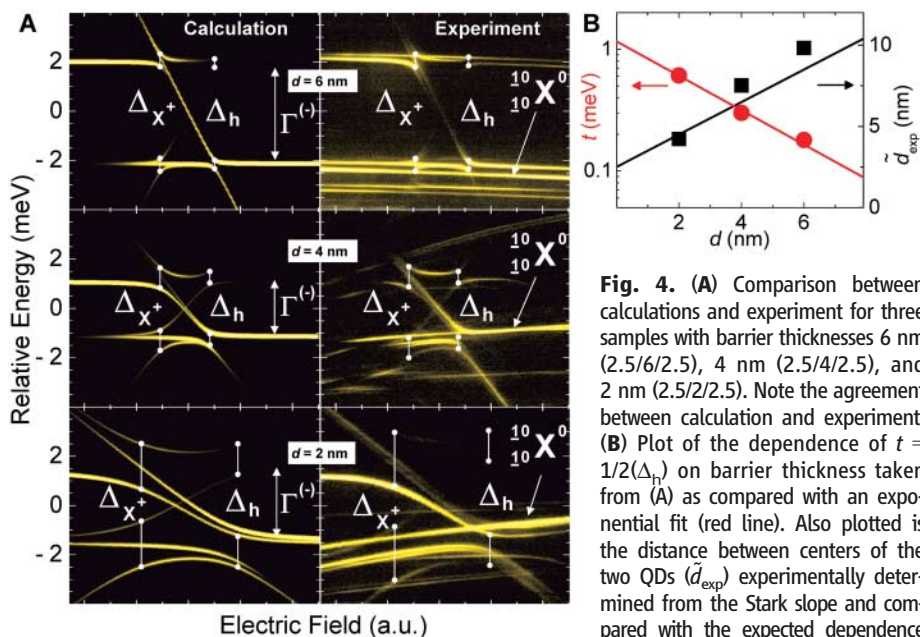**Fig. 4.** (**A**) Comparison between calculations and experiment for three samples with barrier thicknesses 6 nm (2.5/6/2.5), 4 nm (2.5/4/2.5), and 2 nm (2.5/2/2.5). Note the agreement between calculation and experiment. (**B**) Plot of the dependence of $t = 1/2(\Delta_h)$ on barrier thickness taken from (A) as compared with an exponential fit (red line). Also plotted is the distance between centers of the two QDs ($\tilde{d}_{exp}$) experimentally determined from the Stark slope and compared with the expected dependence (black line), $[d + (h_B + h_T)/2]$. The parameters used in the calculations were taken from the following measured values: $(\Delta_h, \Delta_{X^+}, \Gamma^{(-)})_{6nm} = (0.36, 0.70, 4.17)$ meV, $(\Delta_h, \Delta_{X^+}, \Gamma^{(-)})_{4nm} = (0.60, 0.89, 2.24)$ meV, and $(\Delta_h, \Delta_{X^+}, \Gamma^{(-)})_{2nm} = (1.22, 2.26, 2.97)$ meV. a.u., arbitrary units.

electronic spin (8–10); however, unlike electrons, holes should not have strong hyperfine interactions.

30. We thank S. C. Badescu for helpful discussions. This work was supported by the Defense Advanced Research Projects Agency/Quantum Information Science and Technology, National Security Agency/Army Research Office, U.S. Civilian Research and Development Foundation, Russian Foundation for Basic Research, Russian Science Support Foundation, and Office of Navy Research. E.A.S., I.V.P., M.E.W., and M.F.D. are National Research Council/Naval Research Laboratory Research Associates.

Plasticization-Enhanced Hydrogen Purification Using Polymeric Membranes

Haiqing Lin,[1,2] Elizabeth Van Wagner,[1] Benny D. Freeman,[1]* Lora G. Toy,[3] Raghubir P. Gupta[3]

Polymer membranes are attractive for molecular-scale separations such as hydrogen purification because of inherently low energy requirements. However, membrane materials with outstanding hydrogen separation performance in feed streams containing high-pressure carbon dioxide and impurities such as hydrogen sulfide and water are not available. We report highly permeable, reverse-selective membrane materials for hydrogen purification, as exemplified by molecularly engineered, highly branched, cross-linked poly(ethylene oxide). In contrast to the performance of conventional materials, we demonstrate that plasticization can be harnessed to improve separation performance.

Hydrogen is produced primarily by steam reforming of hydrocarbons followed by the water-gas shift reaction, which yields a hydrogen product containing impurities such as CO_2, H_2S, and H_2O (1). The hydrogen must be purified for further use, and based on the high volumes currently produced and the likelihood for this production to increase, even a small improvement in H_2 purification efficiency could substantially reduce the costs. Membrane technology is attractive for molecular-scale separations because of inherent advantages such as high energy efficiency, excellent reliability, and a small footprint (2–5). The potential applicability of membrane technology relies strongly on the ability of membrane materials to exhibit high separation performance at practical feed conditions (e.g., with feed streams that contain high-pressure CO_2 and impurities such as H_2S and H_2O).

Highly permeable and highly selective membrane materials are desired for CO_2/H_2 separation. Gas permeability P, which is the steady-state, pressure- and thickness-normalized gas flux through a membrane, is usually expressed as $P = S \times D$, the product of gas solubility S and gas diffusivity D in the polymer membrane (6). Selectivity $\alpha_{A/B}$, which charac- terizes the ability of a membrane to separate gases A and B, is given by

$$\alpha_{A/B} = \frac{P_A}{P_B} = \frac{S_A}{S_B} \times \frac{D_A}{D_B} \qquad (1)$$

where S_A/S_B is the solubility selectivity and D_A/D_B is the diffusivity selectivity (6). The selectivity of CO_2 over H_2, α_{CO_2/H_2}, reflects the tradeoff between favorable solubility selectivity (CO_2 is more condensable than H_2 and, therefore, $S_{CO_2}/S_{H_2} > 1$) and unfavorable diffusivity selectivity (CO_2 is larger than H_2, so $D_{CO_2}/D_{H_2} < 1$) (7). In conventional polymeric membrane materials (8) and those based on carbon (4) and silica (9, 10), overall gas selectivity is dominated by diffusivity selectivity and, therefore, these materials are typically more permeable to H_2 than to CO_2. Consequently, the H_2 product is produced in the permeate at low pressure, even though further downstream utilization requires H_2 at high pressure. Expensive recompression of the H_2 product hence diminishes the advantage of membrane technology relative to that of conventional separation technologies, such as pressure swing adsorption, that produce H_2 at or near feed pressure (1, 2, 6). To minimize or avoid H_2 recompression, optimal membrane materials should be reverse selective (i.e., more permeable to larger molecules, such as CO_2, than to smaller molecules, such as H_2). Here, we propose that to achieve very high CO_2/H_2 selectivity, a membrane must exhibit favorable interactions with CO_2 to enhance solubility selectivity and have very weak size-sieving ability to bring D_{CO_2}/D_{H_2} as close to 1 as possible. Guided by these material design principles, we prepared and characterized a family of highly branched polymers based on poly(ethylene oxide) (PEO) and found that these polymers display excellent CO_2/H_2 separation performance. Counterintuitively, the CO_2/H_2 selectivity and CO_2 permeability improve as CO_2 partial pressure increases (i.e., as CO_2 concentration sorbed in the polymer increases). This is in contrast to the behavior of conventional, strongly size-selective materials, for which raising CO_2 partial pressure typically decreases selectivity (11).

In a recent review of the influence of primary chemical structure on CO_2/H_2 separation properties of polymers, ethylene oxide (EO) units were identified as the best chemical groups for such membranes because the polar ether oxygens in EO units interact favorably with CO_2, resulting in high solubility selectivity (12). Polymers containing EO can be highly flexible, leading to weak size-sieving behavior and high diffusion coefficients, two factors which contribute directly to high CO_2 permeability and high CO_2/H_2 selectivity (12, 13). However, pure PEO exhibits very low CO_2 permeability [approximately 12 Barrers (14) at 35°C and infinite dilution] as a result of high crystallinity levels (7). Additionally, the presence of crystalline regions in pure PEO reduces polymer chain mobility in the amorphous phase and increases size-sieving ability, thereby decreasing CO_2/H_2 selectivity (12). To circumvent this limitation and effectively frustrate crystallization, short non-PEO segments are introduced into the polymer backbone to interrupt the EO repeat units. Chain branches containing short, noncrystallizable segments of EO are also introduced randomly into the chain backbone to further inhibit crystallinity. This leads to amorphous materials with higher gas permeability and higher CO_2/H_2 selectivity than semicrystalline PEO. Plasticization further improves their CO_2/H_2 separation properties, in contrast to the view that plasticization always reduces polymer membrane separation performance, as it does in the case of CO_2/CH_4 separation in natural gas purification (15). Moreover, all polymers are more permeable to CO_2 than to CH_4 because CO_2 has higher diffusivity (because of its smaller molecular size) and higher solubility (because of its greater tendency to condense) than CH_4. In contrast, polymers that are more permeable to CO_2 than to H_2 are much rarer because the smaller size of H_2 favors its permeation over that of the larger CO_2.

[1]Center for Energy and Environmental Resources and Department of Chemical Engineering, University of Texas, Austin, TX 78758, USA. [2]Membrane Technology and Research, 1360 Willow Road, Suite 103, Menlo Park, CA 94025, USA. [3]Center for Energy Technology, Research Triangle Institute, Research Triangle Park, NC 27709, USA.

*To whom correspondence should be addressed. E-mail: freeman@che.utexas.edu